Optimal shape design in biomimetics based on homogenization and adaptivity

Ronald H.W. Hoppe [a,b], Svetozara I. Petrova [a,c,*]

[a] *Institute of Mathematics, University of Augsburg, D-86159 Augsburg, Germany*
[b] *Department of Mathematics, University of Houston, Houston, TX 77204-3008, Germany*
[c] *CLPP, Bulgarian Academy of Sciences, Block 25A, 1113 Sofia, Bulgaria*

1. Introduction

Biomimetics is a relatively young multidisciplinary science being systematically and intensively developed in the last decade. The concept of implementing ideas from nature is rather old but due to the modern technologies nowadays the material synthesis from biological structures becomes of strongly increasing interest for advanced processing of technological devices. In contrast to engineering materials, biological structures are often microstructural designed materials which exhibit a hierarchically built anatomy,

* Corresponding author. Tel.: +49-821-5982312; fax: +49-821-5982339.
E-mail address: petrova@math.uni-augsburg.de (S.I. Petrova).

developed and optimized in a long-term genetic evolution process. They possess an excellent strength at low density, high stiffness and elasticity, and damage tolerance both on the micro and macro level.

In particular, novel microcellular ceramics with unidirectional porous structures have recently been manufactured from natural grown plant preforms like wood (see, e.g. [9,15,18,19]). The natural wood morphologies are characterized by an open porous system of tracheidal cells which provide the transportation path for water and minerals in the living plants. The inherent cellular highly open porous system, accessible for infiltration of various liquid or gaseous metals, is used for design of the biomorphic porous ceramics. The transformation of the carbonized wood into porous carbide ceramics is done by infiltration-reaction processes with various carbide forming metals (e.g., Si, Ti).

The main scope of this paper focuses on the modelling, simulation, and shape optimization of the novel microstructured biomorphic ceramic materials. The mechanical behavior of the final ceramic workpiece is determined by the geometry of its microstructure which can be very precisely tuned during the processing. Our purpose is to find the microstructural characteristics in order to achieve an optimal mechanical performance of the final product with respect to some optimal criteria and specific applications. In principal, the main efforts in shape optimization problems are addressed to the geometry of the structure as a design variable which means, in particular, that the discretization model associated with the structure has to be changed in the process of optimization. For details, we refer to [2,6,7,20] and the literature therein.

Our shape optimization problem is based on the homogenization approach for modelling of linearly elastic microstructures with a distribution of various material phases. A simple unit microstructure is defined and supposed to be periodically distributed through the design media. The homogenization is possible under the assumption for separation of the microstructure scale from the macroscopic one through an asymptotic expansion (see, e.g. [1,3,5,7,17,20]). The desired properties are specified as a set of equality and inequality constraints. The physical quantities (displacements in terms of the elasticity equation) serve as *state variables* whereas the microscopic geometric widths of layers are considered as *design parameters* within the optimization procedure. In addition, the orientation of the microstructure is important for the final macroscopic problem, i.e., the angle of cell rotation as a design parameter is also taken into account.

In the optimization algorithm, we were typically faced with constrained nonconvex minimization problems with both equality and inequality constraints on the state variables and design parameters. After discretization, for example, by finite elements, we solve the discretized optimization problems by primal–dual interior-point methods which have been recently successfully applied to nonlinear programming problems (cf., e.g. [4,8,11,13,14]). In traditional design optimization strategies the optimization process and the numerical solution of the state equation are separated. We strongly emphasize on the use of the one-shot method (all-in-one approach) where the iterative solution of the discretized state equation is an integral part of the optimization routine.

The remaining part of the present study is organized as follows. In Section 2, the processing scheme of the novel biomorphic ceramics is described. The shape optimization problem is discussed in detail in Section 3. Our purpose is to minimize the objective functional (for instance, the mean compliance) subject to: (i) the homogenized equilibrium equation; (ii) the equality constraint on the solid material part; (iii) the inequality constraints on the design parameters. Primal–dual Newton-type interior-point algorithm is applied in Section 4 to solve the discretized optimization problem. The inequality constraints are treated indirectly as equalities and nonnegative slack variables. Adaptive grid refinement on the basis of a posteriori error estimators has been recently applied in finite element analysis in elasticity (cf., e.g., [10,12,17]). In the numerical experiments given in the last section, we have used an adaptivity in the

microstructure around the domain geometric singularities and across the material interfaces due to the strongly varying material characteristics. To find the effective (homogenized) properties of the composite materials, we have followed the idea of *Zienkiewicz–Zhu* (see [22]) to compute the recovered stresses in terms of elasticity equations.

2. Processing scheme by biotemplating

A particular area within the field of biomimetics is the recent production of biomorphic silicon carbide (SiC) ceramics from natural grown materials like wood and cellulose fibres (see [15,18]). The production process of the ceramic materials relies on the *biotemplating* as a novel technology in the field of biomimetics which features a material synthesis from biologically grown materials into ceramic composites by fast high-temperature processing. The preparation includes basically two processing steps. Firstly, the workpiece of natural wood is dried and preprocessed by high-temperature pyrolysis (800–1800 °C) in inert atmosphere resulting in a biological porous carbon preform (also called carbonized biotemplate). The porosity of the carbon preform is about 20–25% higher than of the dried wood. Due to the high porosity, the pyrolyzed template is infiltrated in the next step with liquid or gaseous silicon (Si) at 1600°C. The silicon reacts with the carbon to finally yield a porous SiC-ceramic material (cf. Fig. 1). The remaining silicon in the tracheidal cells can be removed by chemical etching to increase the porosity. The total porosity of the SiC ceramics strongly depends on the initial cellular structure. The processing scheme is explained in Fig. 2. For details of the high-temperature material synthesis we refer, for example, to [19].

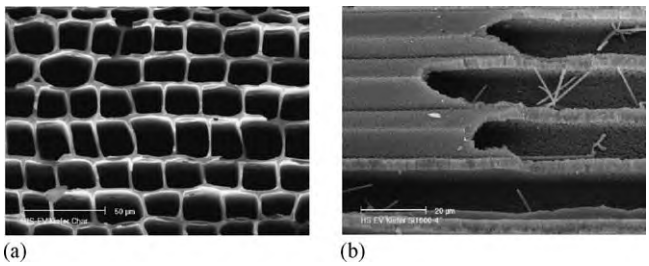

Fig. 1. Microcellular SiC ceramic derived from pine wood, pyrolysis at 1600°/4 h: (a) radial direction; (b) axial direction.

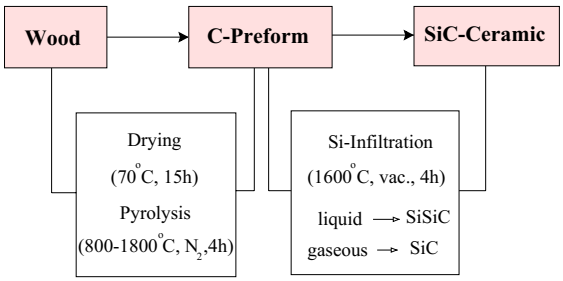

Fig. 2. Processing scheme of microcellular SiC and SiSiC ceramics from wood.

The new anisotropic biomorphic microcellular SiC ceramics cannot be considered furthermore as wood but have a unique oriented cellular microstructure pseudomorphous to wood. In particular, during the high-temperature processing, the microstructural properties of the bioorganic preforms retain and the original wood structure is reproduced almost one-to-one. Moreover, strength and elastic modulus of the pyrolyzed carbon preform and of the final SiC ceramic were derived from stress–strain measurements in different loading directions (e.g., axial, radial, and tangential).

The composite materials described above possess excellent structural–mechanical properties and have received in the last few years a wide range of interest in many technical applications such as heat insulation, substrates, filter and catalyst carriers at high temperature, thermally and mechanically loaded light-weight structures, as well as medical implant structures (e.g., porous materials for bone substitution).

3. Shape optimization by a homogenization

This section deals with the optimal performances of the composite SiC-ceramic materials taking into account the microstructural geometric features that strongly influence the macrocharacteristics of the final product. For structural design purposes there is a need to provide a macroscopic scale model which contains details for the microscopic fine structure as design parameters. The optimal shape design of microstructured materials by homogenization modelling is well established in structural mechanics (cf., e.g. [1–3,5,7,20]). Shape optimization can be realized under the assumption that the original topology of the domain is fixed during the design processing but the geometry of the structure is not fixed, i.e., it changes at each iterative step within the optimization (see [7]).

Our macroscale homogenized model is provided by the homogenization approach assuming a periodical distribution of the microstructure with a geometrically simple infinitesimal tracheidal cell. We consider a unit square periodicity cell Y (see Fig. 3) consisting of an outer layer of carbon, interior layer of SiC, a very thin layer of silicon dioxide (SiO_2), and a void. Experimental data show that the SiC ceramics are not stable under oxidizing conditions and they form a SiO_2 layer of thickness approximately 100 nm whereas the maximum diameter of the tracheidal cell is in the range of 50 μm for pine up to 350 μm for oak. The SiO_2 coating on the interface between the SiC and the void can be done by posttreatment of the ceramic material at 800–1200°C in ambient atmosphere. This very thin microstructural layer on the inner SiC surfaces acts as an oxidation protection layer and inhibits further oxidation.

Let $\Omega \subset \mathcal{R}^2$ be a bounded domain occupied by a SiC-based composite material of periodically distributed constituents. Suppose that the boundary $\partial\Omega = \Gamma_D \cup \Gamma_T$, $\Gamma_D \cap \Gamma_T = \emptyset$, meas $\Gamma_D > 0$. Homogenization is possible if the macro and micro scales are well separated, i.e., we assume that the

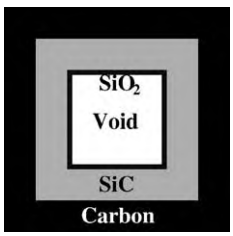

Fig. 3. The periodicity cell Y with three constituents and a void.

periodic cells in the macrostructure are infinitely many but infinitely small and repeated periodically through the medium. We introduce two space variables x (macroscopic variable) and y (microscopic variable) and denote by $\varepsilon := x/y \ll 1$ the *scale parameter* (dimensionless number) which, in fact, represents the periodicity under the assumption that ε is very small with respect to the size of Ω. The parameter ε allows us to define macrofunctions in terms of the microstructural behavior and vice versa. Thus, for any state function $f(y) := f(x/\varepsilon)$, one can compute the spatial derivatives by using the following differentiation rule

$$\frac{\mathrm{d}}{\mathrm{d}x} f\left(x, \frac{x}{\varepsilon}\right) = \frac{\partial f(x, y)}{\partial x} + \varepsilon^{-1} \frac{\partial f(x, y)}{\partial y}.$$

We assume linearly elastic constituents and consider the following elasticity equation in Y

$$-\mathrm{div}\, \boldsymbol{\sigma}(y) = \boldsymbol{F}(y), \quad \text{in } Y \tag{1}$$

with a load vector $\boldsymbol{F}$. Denote by $\boldsymbol{\sigma}(y) = \{\sigma_{ij}(y)\}$, $i, j = 1, 2$, the symmetric stress tensor, by $\boldsymbol{u}(y) = (u_1(y), u_2(y))^{\mathrm{T}}$, $\boldsymbol{u} \in \boldsymbol{H}^1(Y)$, the corresponding displacement vector at point y of the body, and by

$$e_{ij}(\boldsymbol{u}(y)) = \frac{1}{2}\left(\frac{\partial u_i(y)}{\partial y_j} + \frac{\partial u_j(y)}{\partial y_i}\right) \tag{2}$$

the components of the symmetric strain tensor. The problem (1) is subject to periodic boundary conditions on the outer part of ∂Y, Neumann boundary conditions around the hole, and continuity conditions $[\boldsymbol{u}] = 0$ and $[\boldsymbol{\sigma} \cdot \boldsymbol{n}] = 0$ on the interfaces between the layers. The symbol $[\,]$ denotes the jump of the function across the corresponding interface with a normal vector $\boldsymbol{n}$ (cf., e.g. [1]).

Assume that our composite microstructure is governed by the linearized Hooke's law as the constitutive equation which can be written in tensor notations as follows

$$\sigma_{ij}(y) = E_{ijkl}(y) e_{kl}(\boldsymbol{u}(y)). \tag{3}$$

Here, the Einstein summation convention is applied. The *elasticity* (also called *plain stress*) *tensor* $\boldsymbol{E}(y) = (E_{ijkl}(y))$, $i, j, k, l = 1, 2$, of order 4, characterizes the behavior of the material at point y and depends on material constants like Young's modulus and Poisson's ratio. It can be chosen either for the plane stresses or for the plane strains depending on the macroscopic structure to be designed. Note that the elasticity tensor $\boldsymbol{E}(y)$ is zero if y is located in the hole (see Fig. 3) and coincides with the elasticity tensor of the material (carbon, SiC, SiO_2) if y is located in the corresponding layer. The elasticity tensor is symmetric in the following sense

$$E_{ijkl} = E_{jikl} = E_{ijlk} = E_{klij}, \quad \forall\, i, j, k, l = 1, 2 \tag{4}$$

and satisfies the following *ellipticity conditions*

$$E_{ijkl}\, \chi_{ij} \chi_{kl} \geq c\, \chi_{ij}^2, \quad \forall\, \chi_{ij} = \chi_{ji},$$

for a constant $c > 0$ (cf., e.g. [1,3,5,7,17,20]).

Denote by $\boldsymbol{u}_\varepsilon(x) := \boldsymbol{u}(x/\varepsilon)$ the unknown macroscopic displacement vector and consider the following problem

$$-\mathrm{div}\, \boldsymbol{\sigma}_\varepsilon(x) = \boldsymbol{f}(x), \quad \text{in } \Omega, \tag{5}$$

subject to a macroscopic body force $\boldsymbol{f}$ and a macroscopic surface traction $\boldsymbol{q}$ applied to the portion $\Gamma_{\mathrm{T}} \subset \partial\Omega$. Here, $\boldsymbol{\sigma}_\varepsilon(x) := \boldsymbol{E}_\varepsilon(x) \boldsymbol{e}(\boldsymbol{u}_\varepsilon(x))$ is the stress tensor and $\boldsymbol{E}_\varepsilon(x) := \boldsymbol{E}(x/\varepsilon) = \boldsymbol{E}(y)$ is the piecewise

constant elasticity tensor defined in Y. Following [3] for the basic concepts of the homogenization method, the unknown displacement vector is expanded asymptotically as

$$\boldsymbol{u}_\varepsilon(x) = \boldsymbol{u}^{(0)}(x, y) + \varepsilon\, \boldsymbol{u}^{(1)}(x, y) + \cdots, \qquad y = x/\varepsilon, \tag{6}$$

where $\boldsymbol{u}^{(i)}(x, y)$, $i \geq 0$, are Y periodic in y, i.e., take equal values on opposite sides of Y.

The homogenization method requires to find the functions $\boldsymbol{\xi}^{kl} = (\xi_1^{kl}, \xi_2^{kl})$, $k, l = 1, 2$, satisfying the following problem in a weak formulation

$$\int_Y \left(E_{ijpq}(y) \frac{\partial \xi_p^{kl}}{\partial y_q} \right) \frac{\partial \phi_i}{\partial y_j}\, \mathrm{d}y = \int_Y E_{ijkl}(y) \frac{\partial \phi_i}{\partial y_j}\, \mathrm{d}y \tag{7}$$

for an arbitrary Y-periodic variational function $\boldsymbol{\phi} \in \boldsymbol{H}^1(Y)$. After computing the microscopic displacement field $\boldsymbol{\xi}^{kl}$ from (7), we can define the homogenized (effective) coefficients by the following homogenized formulas (we refer to [1,3,5] for details)

$$E_{ijkl}^H = \frac{1}{|Y|} \int_Y \left(E_{ijkl}(y) - E_{ijpq}(y) \frac{\partial \xi_p^{kl}}{\partial y_q} \right) \mathrm{d}y. \tag{8}$$

Due to the symmetry conditions (4), the 4th order homogenized elasticity tensor $\boldsymbol{E}^H = (E_{ijkl}^H)$, $i, j, k, l = 1, 2$, can be written as a symmetric 3×3 matrix

$$\boldsymbol{E}^H = \begin{pmatrix} E_{1111}^H & E_{1122}^H & 0 \\ E_{2211}^H & E_{2222}^H & 0 \\ 0 & 0 & E_{1212}^H \end{pmatrix}. \tag{9}$$

The computation of the homogenized elasticity coefficients can be done analytically for some specific geometries as, for instance, layered materials or checkerboard structures (cf., e.g. [1,3,5]). In case of more complicated microstructures, the computation of E_{ijkl}^H has to be done numerically through a suitable microscopic modelling.

To the microscopic problem (1) on the unit cell Y one can now associate a homogenized problem at the macroscopic level as follows

$$-\mathrm{div}\, \boldsymbol{\sigma}(x) = \boldsymbol{f}(x), \quad \text{in } \Omega, \tag{10}$$

where $\boldsymbol{\sigma}(x) := \boldsymbol{E}^H \boldsymbol{e}(\boldsymbol{u}^{(0)}(x))$, $x \in \Omega$, and $\boldsymbol{E}^H$ stands for the homogenized elasticity tensor (9). Both problems constitute the necessary and sufficient conditions obtained by a suitable limit process where the scale parameter ε tends to zero.

We attempt to optimize mechanical performances of the ceramic composites in terms of an objective functional J which can be chosen according to various merit criteria depending on the application (see, e.g. [2] for details). For this purpose, we have to take into account the technological and problem specific constraints on the state variables (in our case the displacements vector $\boldsymbol{u} = (u_1, u_2)^{\mathrm{T}}$) and the design parameters $\boldsymbol{\alpha} = (\alpha_1, \alpha_2, \ldots, \alpha_m)^{\mathrm{T}}$ (widths of the different material layers) for a number of layers $m > 0$.

We consider as well the angle of cell rotation as an additional design parameter in the shape optimization problem. Note that in this case there are explicit formulas for the computation of the rotated homogenized

elasticity coefficients given by

$$E^R_{ijkl}(\boldsymbol{\alpha}, \theta) = \sum_{m,n,p,q=1}^{2} E^H_{mnpq}(\boldsymbol{\alpha})\, R_{im}(\theta)\, R_{jn}(\theta)\, R_{kp}(\theta)\, R_{lq}(\theta), \tag{11}$$

where $R_{jn}(\theta)$, $1 \le j, n \le 2$, are the components of the rotation matrix and θ is the angle of cell rotation with respect to a fixed reference frame (for instance, the coordinate system) (see also [20]).

Our optimization problem has the form

$$J(\boldsymbol{u}, \boldsymbol{\alpha}, \theta) = \inf_{\boldsymbol{v}, \boldsymbol{\beta}, \gamma} J(\boldsymbol{v}, \boldsymbol{\beta}, \gamma), \tag{12}$$

subject to the following equality and inequality constraints on the state variables and the design parameters:

$$\sum_{i,j,k,l=1}^{2} \int_{\Omega} E^R_{ijkl}(\boldsymbol{\alpha}, \theta) \frac{\partial u_k}{\partial x_l} \frac{\partial \phi_i}{\partial x_j}\, \mathrm{d}x = \int_{\Omega} \boldsymbol{f} \cdot \boldsymbol{\phi}\, \mathrm{d}x + \int_{\Gamma_{\mathrm{T}}} \boldsymbol{q} \cdot \boldsymbol{\phi}\, \mathrm{d}s, \quad \forall\, \boldsymbol{\phi} \in V_0 \tag{13}$$

$$g(\boldsymbol{\alpha}) := \sum_{i=1}^{m} \alpha_i = C; \quad \alpha_{\min} \le \alpha_i \le \alpha_{\max}, \quad 1 \le i \le m, \tag{14}$$

where (in case of unit cell with a square hole located at the center) $\alpha_{\min} = 0$, $\alpha_{\max} = 0.5$, and C, $0 \le C \le 0.5$, is a given constant. Note that $\alpha_i = 0$, $1 \le i \le m$, corresponds to a complete void, $C = 0.5$ to a complete solid material, and the case $0 < \alpha_i$, $C < 0.5$ corresponds to a microstructural porous composite with a void. Eq. (13) refers to the *homogenized equilibrium equation* given in a weak formulation for the space $V_0 := \{\boldsymbol{v} \in \boldsymbol{H}^1(\Omega) | \boldsymbol{v} = \boldsymbol{0} \text{ on } \Gamma_{\mathrm{D}}\}$. Note that the latter is solved at each step within the design optimization procedure, so that one needs a reliable and efficient solver for this equation.

As an objective function in the numerical experiments given in Section 5, we consider the mean compliance of the structure defined as the work done by the loads, namely

$$J(\boldsymbol{u}, \boldsymbol{\alpha}, \theta) := \int_{\Omega} \boldsymbol{f} \cdot \boldsymbol{u}\, \mathrm{d}x + \int_{\Gamma_{\mathrm{T}}} \boldsymbol{q} \cdot \boldsymbol{u}\, \mathrm{d}s. \tag{15}$$

In engineering problems, the compliance is often used as a measure of the stiffness of the system: minimum compliance corresponds to maximum global stiffness and rigidity with respect to the external loads.

4. The optimization procedure

Primal–dual interior-point methods are attractive solvers for optimization problems of type (12)–(14). They are based on iterative procedures which at each iterate generate approximations to solutions that are strictly feasible with respect to the bound constraints. For recent applications of these methods to nonlinear programming we refer the reader, for instance, to [4,8,11,13,14].

We deal with the inequality constraints by introducing nonnegative slack variables $\boldsymbol{s}, \boldsymbol{t} \in \mathcal{R}^m$. This variant of the primal–dual approach is associated with a small amount of additional work and storage, since the slacks do not enter the objective function and are constrained by simple bounds (cf., e.g. [8,11]). The discretized nonlinear constrained minimization problem has the form

$$J(\boldsymbol{u}, \boldsymbol{\alpha}, \theta) = \inf_{\boldsymbol{v}, \boldsymbol{\beta}, \gamma} J(\boldsymbol{v}, \boldsymbol{\beta}, \gamma), \tag{16}$$

subject to

$$\begin{aligned} A(\boldsymbol{\alpha},\theta)\,\boldsymbol{u}-\boldsymbol{b}=0, \qquad & \alpha_{\min}\boldsymbol{e}-\boldsymbol{\alpha}+\boldsymbol{s}=0, \qquad \boldsymbol{s}\geq 0;\\ g(\boldsymbol{\alpha})-C=0, \qquad & \boldsymbol{\alpha}-\alpha_{\max}\boldsymbol{e}+\boldsymbol{t}=0, \qquad \boldsymbol{t}\geq 0; \end{aligned} \tag{17}$$

where $\boldsymbol{e}\in\mathcal{R}^m$, $\boldsymbol{e}=(e_1,\ldots,e_m)^{\mathrm{T}}$, $e_i=1,\ 1\leq i\leq m$, $A(\boldsymbol{\alpha},\theta)$ is the stiffness matrix corresponding to (13), and $\boldsymbol{b}$ is the discrete load vector. The inequalities in (17) are treated componentwise.

The *Lagrangian function* associated with problem (16)–(17) is

$$\begin{aligned} \mathcal{L}(\boldsymbol{u},\boldsymbol{\alpha},\theta,\boldsymbol{\lambda},\eta,\boldsymbol{z},\boldsymbol{w},\boldsymbol{s},\boldsymbol{t},\boldsymbol{k},\boldsymbol{p}) := \quad & J(\boldsymbol{u},\boldsymbol{\alpha},\boldsymbol{\theta})\\ & +\boldsymbol{\lambda}^{\mathrm{T}}(\mathrm{A}(\boldsymbol{\alpha},\boldsymbol{\theta})\boldsymbol{u}-\boldsymbol{b})+\eta\,(g(\boldsymbol{\alpha})-C) \qquad (18)\\ & +\boldsymbol{z}^{\mathrm{T}}(\alpha_{\min}\boldsymbol{e}-\boldsymbol{\alpha}+\boldsymbol{s})+\boldsymbol{w}^{\mathrm{T}}(\boldsymbol{\alpha}-\alpha_{\max}\boldsymbol{e}+\boldsymbol{t})\\ & -\boldsymbol{k}^{\mathrm{T}}\boldsymbol{s}-\boldsymbol{p}^{\mathrm{T}}\boldsymbol{t}. \qquad (19) \end{aligned}$$

Here, $\boldsymbol{\lambda}$, η, $\boldsymbol{z}$, $\boldsymbol{w}$, and $\boldsymbol{k}$, $\boldsymbol{p}\in\mathcal{R}^m$, $\boldsymbol{k}\geq 0$, $\boldsymbol{p}\geq 0$, are the Lagrange multipliers for the equality and inequality constraints in (17), respectively. Our purpose is to find an isolated (locally unique) local minimum of (16)–(17) under the assumption that at least one such point exists. We suppose that the standard conditions for the application of Newton's method, see, e.g. [4], are satisfied.

Denote by $\boldsymbol{\Phi} := (\boldsymbol{u},\boldsymbol{\alpha},\theta,\boldsymbol{\lambda},\eta,\boldsymbol{z},\boldsymbol{w},\boldsymbol{s},\boldsymbol{t},\boldsymbol{k},\boldsymbol{p})$ the vector of unknown variables. The interior-point method is characterized by substituting the complementarity conditions $K\boldsymbol{s}=\boldsymbol{0}$ and $P\boldsymbol{t}=\boldsymbol{0}$ by the *perturbed complementarity conditions* $K\boldsymbol{s}=\rho\boldsymbol{e}$ and $P\boldsymbol{t}=\rho\boldsymbol{e}$ for a suitably chosen perturbation parameter ρ, $0\leq\rho\leq 1$, and diagonal matrices $K=\mathrm{diag}(k_i)$ and $P=\mathrm{diag}(p_i)$.

The Karush–Kuhn–Tucker (KKT) first-order necessary conditions for optimality result in the following nonlinear equation for the unknown variables:

$$F^{(\rho)}(\boldsymbol{\Phi}) := \begin{pmatrix} \nabla_{\boldsymbol{u}}\mathcal{L}\\ \nabla_{\boldsymbol{\alpha}}\mathcal{L}\\ \nabla_{\theta}\mathcal{L}\\ \nabla_{\boldsymbol{\lambda}}\mathcal{L}\\ \nabla_{\eta}\mathcal{L}\\ \nabla_{\boldsymbol{z}}\mathcal{L}\\ \nabla_{\boldsymbol{w}}\mathcal{L}\\ \nabla_{\boldsymbol{s}}\mathcal{L}\\ \nabla_{\boldsymbol{t}}\mathcal{L}\\ \nabla_{\boldsymbol{k}}\mathcal{L}\\ \nabla_{\boldsymbol{p}}\mathcal{L} \end{pmatrix} = \begin{pmatrix} \nabla_{\boldsymbol{u}}J+\mathrm{A}(\boldsymbol{\alpha},\theta)^{\mathrm{T}}\boldsymbol{\lambda}\\ \partial_{\boldsymbol{\alpha}}(\boldsymbol{\lambda}^{\mathrm{T}}A(\boldsymbol{\alpha},\theta)\boldsymbol{u})+\eta\nabla g(\boldsymbol{\alpha})-\boldsymbol{z}+\boldsymbol{w}\\ \partial_{\theta}(\boldsymbol{\lambda}^{\mathrm{T}}A(\boldsymbol{\alpha},\theta)\boldsymbol{u})\\ A(\boldsymbol{\alpha},\theta)\boldsymbol{u}-\boldsymbol{b}\\ g(\boldsymbol{\alpha})-\mathrm{C}\\ \alpha_{\min}\boldsymbol{e}-\boldsymbol{\alpha}+\boldsymbol{s}\\ \boldsymbol{\alpha}-\alpha_{\max}\boldsymbol{e}+\boldsymbol{t}\\ \boldsymbol{z}-\boldsymbol{k}\\ \boldsymbol{w}-\boldsymbol{p}\\ K\boldsymbol{s}-\rho\boldsymbol{e}\\ P\boldsymbol{t}-\rho\boldsymbol{e} \end{pmatrix} = \boldsymbol{0}, \tag{20}$$

where $\nabla_{\boldsymbol{k}}\mathcal{L}:=K\boldsymbol{s}-\rho\boldsymbol{e}$ and $\nabla_{\boldsymbol{p}}\mathcal{L}:=P\boldsymbol{t}-\rho\boldsymbol{e}$. The *search direction* is denoted by

$$\Delta\boldsymbol{\Phi} := (\Delta\boldsymbol{u},\Delta\boldsymbol{\alpha},\Delta\theta,\Delta\boldsymbol{\lambda},\Delta\eta,\Delta\boldsymbol{z},\Delta\boldsymbol{w},\Delta\boldsymbol{s},\Delta\boldsymbol{t},\Delta\boldsymbol{k},\Delta\boldsymbol{p})$$

and the update $\boldsymbol{\Phi}\leftarrow\boldsymbol{\Phi}+\Delta\boldsymbol{\Phi}$ is determined by the increment $\Delta\boldsymbol{\Phi}$ computed by using the Newton method for the following ρ-dependent system of equations:

$$\nabla F^{(\rho)}(\boldsymbol{\Phi})\,\Delta\boldsymbol{\Phi}=-F^{(\rho)}(\boldsymbol{\Phi}), \tag{21}$$

where (21) is often referred to as the *primal–dual* system and solved at each iteration with a decreasing parameter ρ. More precisely, (21) is equivalent to

$$\begin{pmatrix} 0 & \mathcal{L}_{u\alpha} & \mathcal{L}_{u\theta} & \mathcal{L}_{u\lambda} & 0 & 0 & 0 & 0 & 0 & 0 & 0 \\ \mathcal{L}_{\alpha u} & \mathcal{L}_{\alpha\alpha} & \mathcal{L}_{\alpha\theta} & \mathcal{L}_{\alpha\lambda} & \mathcal{L}_{\alpha\eta} & -I & I & 0 & 0 & 0 & 0 \\ \mathcal{L}_{\theta u} & \mathcal{L}_{\theta\alpha} & \mathcal{L}_{\theta\theta} & \mathcal{L}_{\theta\lambda} & 0 & 0 & 0 & 0 & 0 & 0 & 0 \\ \mathcal{L}_{\lambda u} & \mathcal{L}_{\lambda\alpha} & \mathcal{L}_{\lambda\theta} & 0 & 0 & 0 & 0 & 0 & 0 & 0 & 0 \\ 0 & \mathcal{L}_{\eta\alpha} & 0 & 0 & 0 & 0 & 0 & 0 & 0 & 0 & 0 \\ 0 & -I & 0 & 0 & 0 & 0 & 0 & I & 0 & 0 & 0 \\ 0 & I & 0 & 0 & 0 & 0 & 0 & 0 & I & 0 & 0 \\ 0 & 0 & 0 & 0 & 0 & I & 0 & 0 & 0 & -I & 0 \\ 0 & 0 & 0 & 0 & 0 & 0 & I & 0 & 0 & 0 & -I \\ 0 & 0 & 0 & 0 & 0 & 0 & 0 & K & 0 & S & 0 \\ 0 & 0 & 0 & 0 & 0 & 0 & 0 & 0 & P & 0 & T \end{pmatrix} \begin{pmatrix} \Delta \boldsymbol{u} \\ \Delta \boldsymbol{\alpha} \\ \Delta \theta \\ \Delta \boldsymbol{\lambda} \\ \Delta \eta \\ \Delta \boldsymbol{z} \\ \Delta \boldsymbol{w} \\ \Delta \boldsymbol{s} \\ \Delta \boldsymbol{t} \\ \Delta \boldsymbol{k} \\ \Delta \boldsymbol{p} \end{pmatrix} = - \begin{pmatrix} \nabla_{\boldsymbol{u}} \mathcal{L} \\ \nabla_{\boldsymbol{\alpha}} \mathcal{L} \\ \nabla_{\theta} \mathcal{L} \\ \nabla_{\boldsymbol{\lambda}} \mathcal{L} \\ \nabla_{\eta} \mathcal{L} \\ \nabla_{\boldsymbol{z}} \mathcal{L} \\ \nabla_{\boldsymbol{w}} \mathcal{L} \\ \nabla_{\boldsymbol{s}} \mathcal{L} \\ \nabla_{\boldsymbol{t}} \mathcal{L} \\ \nabla_{\boldsymbol{k}} \mathcal{L} \\ \nabla_{\boldsymbol{p}} \mathcal{L} \end{pmatrix}, \tag{22}$$

where I stands for the identity matrix, $S = \operatorname{diag}(s_i)$ and $T = \operatorname{diag}(t_i)$ are diagonal matrices.

The primal–dual matrix $\nabla F^{(\rho)}(\boldsymbol{\Phi})$ in (21) is sparse, nonsymmetric, indefinite, and usually well-conditioned, i.e., it has a bounded condition number as $\rho \to 0$. We transform $\nabla F^{(\rho)}(\boldsymbol{\Phi})$ to a smaller (so called *condensed*) symmetric matrix by eliminating the increments for $\boldsymbol{s}$ and $\boldsymbol{t}$ from the 6th and 7th rows of (22). We obtain $\Delta \boldsymbol{s} = \Delta \boldsymbol{\alpha} - \nabla_{\boldsymbol{z}} \mathcal{L}$, $\Delta \boldsymbol{t} = -\Delta \boldsymbol{\alpha} - \nabla_{\boldsymbol{w}} \mathcal{L}$ and involve them in the last two rows of (22) to get

$$\Delta \boldsymbol{k} = S^{-1}(-\nabla_{\boldsymbol{k}} \mathcal{L} - K\,(\Delta \boldsymbol{\alpha} - \nabla_{\boldsymbol{z}} \mathcal{L})), \qquad \Delta \boldsymbol{p} = T^{-1}(-\nabla_{\boldsymbol{p}} \mathcal{L} + P\,(\Delta \boldsymbol{\alpha} + \nabla_{\boldsymbol{w}} \mathcal{L})). \tag{23}$$

The substitution (23) in $\Delta \boldsymbol{z} = \Delta \boldsymbol{k} - \nabla_{\boldsymbol{s}} \mathcal{L}$, $\Delta \boldsymbol{t} = \Delta \boldsymbol{p} - \nabla_{\boldsymbol{t}} \mathcal{L}$ and further in the second row of (22) results in the following linear system

$$\begin{pmatrix} 0 & \mathcal{L}_{u\alpha} & \mathcal{L}_{u\theta} & \mathcal{L}_{u\lambda} & 0 \\ \mathcal{L}_{\alpha u} & \tilde{\mathcal{L}}_{\alpha\alpha} & \mathcal{L}_{\alpha\theta} & \mathcal{L}_{\alpha\lambda} & \mathcal{L}_{\alpha\eta} \\ \mathcal{L}_{\theta u} & \mathcal{L}_{\theta\alpha} & \mathcal{L}_{\theta\theta} & \mathcal{L}_{\theta\lambda} & 0 \\ \mathcal{L}_{\lambda u} & \mathcal{L}_{\lambda\alpha} & \mathcal{L}_{\lambda\theta} & 0 & 0 \\ 0 & \mathcal{L}_{\eta\alpha} & 0 & 0 & 0 \end{pmatrix} \begin{pmatrix} \Delta \boldsymbol{u} \\ \Delta \boldsymbol{\alpha} \\ \Delta \theta \\ \Delta \boldsymbol{\lambda} \\ \Delta \eta \end{pmatrix} = - \begin{pmatrix} \nabla_{\boldsymbol{u}} \mathcal{L} \\ \tilde{\nabla}_{\boldsymbol{\alpha}} \mathcal{L} \\ \nabla_{\theta} \mathcal{L} \\ \nabla_{\boldsymbol{\lambda}} \mathcal{L} \\ \nabla_{\eta} \mathcal{L} \end{pmatrix}, \tag{24}$$

where $\tilde{\mathcal{L}}_{\alpha\alpha} = \mathcal{L}_{\alpha\alpha} + S^{-1}\,K + T^{-1}\,P$ and the modified entry for the right-hand side is

$$\tilde{\nabla}_{\boldsymbol{\alpha}} \mathcal{L} = \nabla_{\boldsymbol{\alpha}} \mathcal{L} + S^{-1}(\nabla_{\boldsymbol{k}} \mathcal{L} - K\,\nabla_{\boldsymbol{z}} \mathcal{L}) + \nabla_{\boldsymbol{s}} \mathcal{L} - T^{-1}(\nabla_{\boldsymbol{p}} \mathcal{L} - P\,\nabla_{\boldsymbol{w}} \mathcal{L}) - \nabla_{\boldsymbol{t}} \mathcal{L}.$$

Transforming iterations, proposed in [21], are applied to compute the search direction. We consider a null space decomposition of the condensed primal–dual matrix by interchanging the second and fourth rows and columns and partition the resulting matrix into 2×2-block structure. Details for the solution procedure can be found in [16].

We use the *line-search* version of the Newton method. At the kth iteration, once the solution $\Delta \boldsymbol{\Phi}^{(k)}$ of (21) has been determined, we find a steplength $\zeta^{(k)} > 0$ such that the next iterate $\boldsymbol{\Phi}^{(k+1)} := \boldsymbol{\Phi}^{(k)} + \zeta^{(k)} \Delta \boldsymbol{\Phi}^{(k)}$

has a progress in minimization. In all Newton-type methods, $\zeta^{(k)} = 1$ is almost always the "ideal" value. The method for choosing $\zeta^{(k)}$ at each iteration becomes more complex, as it is well known that for general nonlinear problems with a poor initial estimate, Newton's method may diverge.

A standard approach for choosing the steplength $\zeta^{(k)}$ is to define a suitable merit function, that measures the progress towards the solution. We consider the l_2 norm of the residual as a merit function

$$M(\boldsymbol{\Phi}^{(k)}) = \|F^{(\rho)}(\boldsymbol{\Phi}^{(k)})\|_2 \tag{25}$$

and try at each iteration k to reduce it in a sense $M(\boldsymbol{\Phi}^{(k+1)}) < M(\boldsymbol{\Phi}^{(k)})$.

For simplicity, we denote the unknown variables by

$$\boldsymbol{x} = (\boldsymbol{u}, \boldsymbol{\alpha}, \theta), \quad \boldsymbol{y} = (\boldsymbol{\lambda}, \eta), \quad \boldsymbol{h} = (\boldsymbol{z}, \boldsymbol{w}), \quad \boldsymbol{r} = (\boldsymbol{s}, \boldsymbol{t}), \quad \boldsymbol{d} = (\boldsymbol{k}, \boldsymbol{p})$$

and the corresponding increments by

$$\Delta\boldsymbol{x} = (\Delta\boldsymbol{u}, \Delta\boldsymbol{\alpha}, \Delta\theta), \quad \Delta\boldsymbol{y} = (\Delta\boldsymbol{\lambda}, \Delta\eta), \quad \Delta\boldsymbol{h} = (\Delta\boldsymbol{z}, \Delta\boldsymbol{w}), \quad \Delta\boldsymbol{r} = (\Delta\boldsymbol{s}, \Delta\boldsymbol{t}), \quad \Delta\boldsymbol{d} = (\Delta\boldsymbol{k}, \Delta\boldsymbol{p}).$$

Instead of one parameter $\zeta^{(k)}$ we allow us various steplengths for each unknown and define a diagonal matrix $\Lambda^{(k)}$ as follows:

$$\Lambda^{(k)} = \operatorname{diag}(\zeta_{\boldsymbol{x}}^{(k)}, \ldots, \zeta_{\boldsymbol{x}}^{(k)}, \zeta_{\boldsymbol{y}}^{(k)}, \ldots, \zeta_{\boldsymbol{y}}^{(k)}, \zeta_{\boldsymbol{h}}^{(k)}, \ldots, \zeta_{\boldsymbol{h}}^{(k)}, \zeta_{\boldsymbol{r}}^{(k)}, \ldots, \zeta_{\boldsymbol{r}}^{(k)}, \zeta_{\boldsymbol{d}}^{(k)}, \ldots, \zeta_{\boldsymbol{d}}^{(k)}).$$

To find the update solution $\boldsymbol{\Phi}^{(k+1)} := \boldsymbol{\Phi}^{(k)} + \Lambda^{(k)}\,\Delta\boldsymbol{\Phi}^{(k)}$ we apply the interior-point algorithm proposed in [11] which is briefly sketched for clearance purposes.

4.1. Primal–dual Newton interior-point algorithm

S0. Choose $\boldsymbol{\Phi}^{(0)} = (\boldsymbol{x}^{(0)}, \boldsymbol{y}^{(0)}, \boldsymbol{h}^{(0)}, \boldsymbol{r}^{(0)}, \boldsymbol{d}^{(0)})$ such that $(\boldsymbol{h}^{(0)}, \boldsymbol{r}^{(0)}, \boldsymbol{d}^{(0)}) > 0$. For $k = 0, 1, 2, \ldots$, do the following steps:

S1. Test for convergence: if $M(\boldsymbol{\Phi}^{(k)}) \le \varepsilon_{\text{exit}}$, stop.

S2. Choose $\rho^{(k)} \in (0, 1)$.

S3. Find the perturbed Newton search direction $\Delta\boldsymbol{\Phi}^{(k)}$ from (21).

S4. Compute the parameters

$$\begin{aligned}
\hat{\zeta}_{\boldsymbol{h}}^{(k)} &= \frac{-1}{\min((H^{(k)})^{-1}\,\Delta\boldsymbol{h}^{(k)}, -1)},\\
\hat{\zeta}_{\boldsymbol{r}}^{(k)} &= \frac{-1}{\min((R^{(k)})^{-1}\,\Delta\boldsymbol{r}^{(k)}, -1)},\\
\hat{\zeta}_{\boldsymbol{d}}^{(k)} &= \frac{-1}{\min((D^{(k)})^{-1}\,\Delta\boldsymbol{d}^{(k)}, -1)},
\end{aligned} \tag{26}$$

where $H^{(k)} = \operatorname{diag}(h_i^{(k)})$, $R^{(k)} = \operatorname{diag}(r_i^{(k)})$, and $D^{(k)} = \operatorname{diag}(d_i^{(k)})$.

S5. For a fixed $\beta \in (0, 1)$, choose $\tau^{(k)} \in (0, 1)$ and $\zeta \in (0, 1]$ satisfying the decrease

$$M(\boldsymbol{\Phi}^{(k)} + \Lambda^{(k)}\,\Delta\boldsymbol{\Phi}^{(k)}) \le M(\boldsymbol{\Phi}^{(k)}) + \beta\zeta\nabla M(\boldsymbol{\Phi}^{(k)})^{\mathrm{T}}\,\Delta\boldsymbol{\Phi}^{(k)},$$

where the steplengths in $\Lambda^{(k)}$ are selected as follows:

$$\zeta_{\boldsymbol{x}}^{(k)} = \zeta, \qquad \zeta_{\boldsymbol{y}}^{(k)} = \zeta,$$

$$\zeta_{\boldsymbol{h}}^{(k)} = \min\left(1, \tau^{(k)}\hat{\zeta}_{\boldsymbol{h}}^{(k)}\right),$$

$$\zeta_{\boldsymbol{r}}^{(k)} = \min\left(1, \tau^{(k)}\hat{\zeta}_{\boldsymbol{r}}^{(k)}\right),$$

$$\zeta_{\boldsymbol{d}}^{(k)} = \min\left(1, \tau^{(k)}\hat{\zeta}_{\boldsymbol{d}}^{(k)}\right).$$

S6. Set $\boldsymbol{\Phi}^{(k+1)} := \boldsymbol{\Phi}^{(k)} + \Lambda^{(k)}\Delta\boldsymbol{\Phi}^{(k)}$ and $k := k + 1$. Go to S1.

It was shown in [11] that for equal steplengths of $\boldsymbol{h}$ and $\boldsymbol{d}$ the iterate $\boldsymbol{\Phi}^{(k)}$ generated by the interior-point algorithm above, gives a descent for the merit function, i.e., $\nabla M(\boldsymbol{\Phi}^{(k)})^{\mathrm{T}}\,\Delta\boldsymbol{\Phi}^{(k)} < 0$.

5. Computational results

In this section, we comment on some computational results concerning the microscopic problem to find the homogenized elasticity coefficients and the macroscopic shape optimization problem. The elasticity Eq. (7) is solved numerically using a conforming finite element discretization of the periodicity cell Y by linear basis functions. Due to the equal solutions $\boldsymbol{\xi}^{12} = \boldsymbol{\xi}^{21}$, one has to solve three problems in the period Y to find $\boldsymbol{\xi}^{11}$ (Problem 1), $\boldsymbol{\xi}^{22}$ (Problem 2), and $\boldsymbol{\xi}^{12}$ (Problem 3). The preconditioned conjugate gradient (PCG) method with an incomplete Cholesky factorization as a preconditioner and an appropriate stopping criterion is applied to solve the discretized problem.

The example problems under consideration treat plane stress linear elasticity. The Young modulus E (in GPa) and the Poisson ratio ν of our three materials are, respectively, $E = 10$, $\nu = 0.22$ for carbon, $E = 410$, $\nu = 0.14$ for SiC, and $E = 70$, $\nu = 0.17$ for SiO_2. Note that in the case of a square hole located at the center of the microcell, the homogenized coefficient $E^H_{2222} = E^H_{1111}$ whereas for a rectangular hole both coefficients differ.

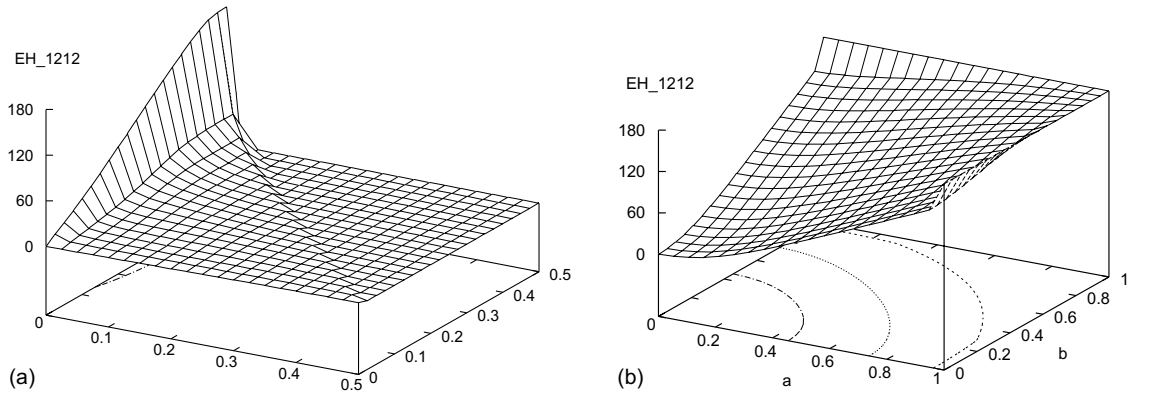

Fig. 4. Homogenized coefficient E^H_{1212}: (a) w.r.t. the widths of carbon and SiC layers (square hole); (b) w.r.t. the sizes $1 - a$ and $1 - b$ of the rectangular hole (pure SiC ceramic).

We assume that the material layers in the periodicity cell shown in Fig. 3 have equal widths from all sides of the cell. Denote by α_i, $i = 1$–3, the widths of the carbon, SiC, and SiO_2 layers, respectively. Fig. 4(a) illustrates the behavior of the homogenized coefficient E^H_{1212} in case of square hole versus α_1 and α_2 which vary between 0 and 0.5. In this example, we do not suppose an additional oxidation as a result of a high-temperature posttreatment of the ceramic material, i.e., we ignore the additional thin layer of SiO_2 and set $\alpha_3 = 0$. Usually, in practice, the hole is located inside the microstructure but we find interesting to demonstrate the behavior, for instance, of E^H_{1212} depending on a rectangular hole $[1 - a] \times [1 - b]$, see Fig. 4(b). Note that $a = b = 0$ represents a complete void, $a = b = 1$ realizes a complete solid material, and $0 < a < 1, 0 < b < 1$ characterize a general porous material. We consider in this example the case when the carbon has completely reacted with the SiC which strongly concerns the so-called *pure biomorphic SiC ceramics*. Very recently, the chemical experiments have shown that the carbon phase limits the mechanical properties of the composite materials and restricts their high-temperature applications. The final transformation of the original carbonized template to pure ceramic composite requires to offer enough silicon during the infiltration process and to wait an appropriate time until the carbon is completely consumed by the silicon resulting in a SiC phase.

For equal widths of layers from all sides of the cell (see Fig. 3), the void area is computed as

$$S_{\text{void}} = \left(1 - 2\sum_{i=1}^{m} \alpha_i\right)^2 \tag{27}$$

and the total material density is denoted by

$$\mu(\boldsymbol{\alpha}) = 1 - S_{\text{void}} = 4\sum_{i=1}^{m} \alpha_i \left(1 - \sum_{i=1}^{m} \alpha_i\right). \tag{28}$$

Fig. 5 displays the dependence of the homogenized elasticity coefficients on the density of the cell. In particular, we show this behavior versus the width of the SiC layer in case of pure SiC ceramics. Note that the density of the tracheidal cells essentially depends on the growth of the tree. In early wood regions (spring, summer) the porosity of the cells is large whereas for late wood regions (autumn, winter) the holes are smaller and the cell walls are thicker. Fig. 5(a) shows the behavior of the effective coefficients for early wood ($0 \le \alpha_2 \le 0.15$, density 51%) and Fig. 5(b) demonstrates the coefficients for late wood ($0 \le \alpha_2 \le 0.3$, density 84%). One can easily observe from both pictures on this figure a highly nonlinear behavior of the homogenized coefficients.

Furthermore, we briefly focus on the necessity of using adaptive mesh refinement around the singularities in the periodic microstructure. Early results of using mesh adaptivity for shape optimization of

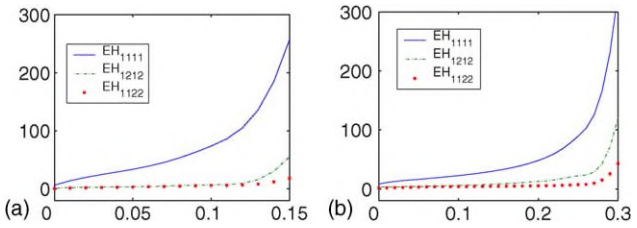

Fig. 5. Homogenized coefficients w.r.t. the width α_2 of SiC layer for pure SiC ceramic: (a) early wood, density 51% and (b) late wood, density 84%.

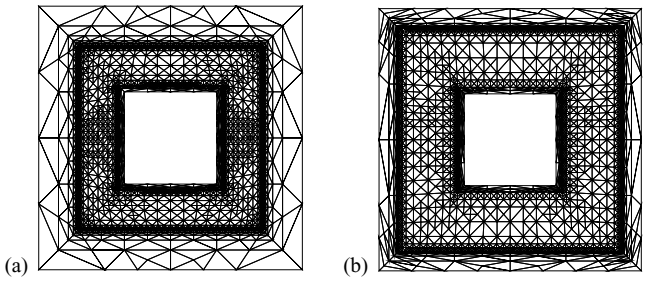

Fig. 6. Problem 1, density = 0.8775; 10 adaptive refinement levels: $\alpha_3 = 0.025$; (a) $\alpha_1 = 0.15$, $\alpha_2 = 0.15$, 5086 triangles, 2562 nodes; (b) $\alpha_1 = 0.075$, $\alpha_2 = 0.3$, 4620 triangles, 2332 nodes.

linearly elastic structures can be found, for example, in [7,17]. In our numerical experiments, we use the *Zienkiewicz–Zhu* (ZZ) a posteriori error estimator, proposed in [22], which has been recently successfully applied to many finite element simulations and widely used in many industrial codes. The main idea of the method consists in computing a more accurate stress tensor by a post-processing and take the difference between this so-called *recovered continuous stress* and the discrete finite element solution stress as an error estimator. In case of linear finite elements, the nodal averaging procedure or the L_2-projection technique is applied to compute the recovered stresses. Averaging techniques in adaptive finite element methods for linear elasticity problems providing reliable and efficient a posteriori error estimators by a simple post-processing are theoretically and numerically discussed, for example, in [10]. For details of performing practical adaptive mesh-refinement procedures we refer to [12].

The adaptive mesh-refinement process concerning our numerical tests is visualized in Figs. 6 and 7. In Fig. 6 we show the adaptive refined grid varying the widths of the material layers. An additional mesh adaptivity is observed across the material interfaces in the microstructure due to the strongly varying material properties (Young's modulus and Poisson's ratio). From Fig. 7(a), one can see that in the case of one material (for example, SiC) an appropriate refinement is done around the corners where the hole with a complete void is located. Table 1 contains the values of the computed average coefficient E^H_{1111} and the number of triangles and nodes for a fixed number of adaptive levels. In Table 2, the values of the homogenized elasticity coefficients on various adaptive refinement levels are presented in the case of early wood (values of the density $\mu = 19$ and 36%).

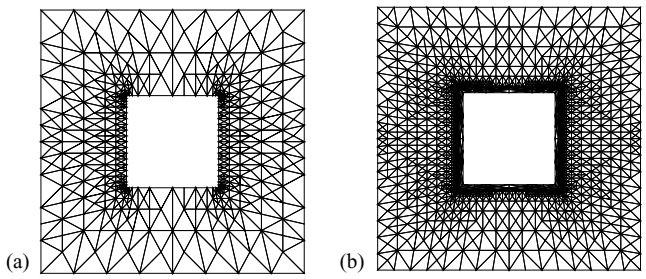

Fig. 7. Problem 1, density = 0.8775; 10 adaptive refinement levels: (a) $\alpha_2 = 0.325$, 846 triangles, 482 nodes; (b) $\alpha_2 = 0.3$, $\alpha_3 = 0.025$, 4177 triangles, 2137 nodes.

Table 1
Homogenized coefficient E^H_{1111} w.r.t. adaptive refinement level, Problem 1, $\mu = 75\%$

Level	# Triangles	# Nodes	E^H_{1111}
1	72	48	43.243
2	96	60	42.685
3	204	114	41.301
4	284	156	39.899
5	532	284	39.090
6	776	406	38.602
7	1284	666	38.095
8	1956	1006	37.785
9	2796	1430	37.615
10	3626	1848	37.427
11	5046	2563	37.245

Table 2
Homogenized coefficients for early wood: density $\mu = 19\%$ ($\alpha_1 = \alpha_2 = 0.025$) and $\mu = 36\%$ ($\alpha_1 = \alpha_2 = 0.05$)

Level	E^H_{1111}	E^H_{1122}	E^H_{1212}	E^H_{1111}	E^H_{1122}	E^H_{1212}
1	105.650	6.489	16.547	85.898	7.856	14.567
2	105.020	6.420	16.493	83.717	7.045	14.370
3	97.249	6.027	13.667	79.060	6.294	12.460
4	95.613	4.834	9.152	73.639	6.058	8.850
5	92.979	3.707	7.186	70.947	5.827	7.078
6	91.636	3.793	5.605	69.022	5.445	6.444
7	89.531	3.134	4.880	66.842	4.625	5.635
8	89.032	2.872	4.228	65.357	4.206	4.826
9	88.116	3.120	3.606	64.350	3.774	4.637
10	85.305	2.539	3.263	63.631	3.396	4.187
11	84.825	2.475	3.181	63.192	3.149	4.116

Table 3
Convergence results for biomorphic microcellular SiC ceramics, $\theta^{(0)} = 0$

$\alpha_1^{(0)}$	$\alpha_2^{(0)}$	C	iter	α_1	α_2	θ	ρ	$\|F^{(\rho)}\|_2$
0.05	0.05	0.3	12	1.24E−14	0.3	0.651	9.25E−23	3.24E−7
0.05	0.25	0.05	12	2.65E−16	0.05	0.587	5.15E−24	4.44E−8
0.1	0.05	0.4	12	4.70E−15	0.4	0.124	1.04E−23	1.73E−7
0.1	0.35	0.05	25	2.91E−15	0.05	0.587	6.22E−22	2.34E−7
0.1	0.2	0.01	12	4.54E−17	0.01	0.563	3.51E−23	1.16E−7
0.1	0.2	0.4	11	2.24E−14	0.4	0.657	1.81E−22	4.50E−7
0.2	0.2	0.05	11	1.91E−14	0.05	2.158	2.70E−20	6.87E−7
0.25	0.05	0.1	16	5.79E−16	0.1	0.611	3.38E−24	6.88E−8
0.3	0.05	0.1	16	1.17E−14	0.1	2.181	1.41E−21	5.55E−7
0.3	0.1	0.03	13	6.00E−18	0.03	9.001	1.27E−26	9.38E−10
0.3	0.1	0.25	11	2.68E−14	0.25	7.740	1.43E−21	8.26E−7

Some computational results on the convergence history of the primal–dual Newton interior-point method applied to our optimization problem are presented in Table 3. We vary the initial widths of layers and the constant C with respect to (14). We report the optimal values of the design parameters, the number of iterations `iter`, the last value of the perturbation parameter ρ and the final value of the merit function M. In order to provide a sufficiently smooth dependence needed whitin the optimization, the homogenized elasticity coefficients $E^H_{ijkl}(\boldsymbol{\alpha})$ are computed for sampling values of $\boldsymbol{\alpha}$ varying on a uniform grid and determined as the multivariate cubic spline interpolant with respect to the appropriately chosen partition. This approach allows us to compute the first and second derivatives of the Lagrangian function needed at each iterate of the optimization loop.

6. Concluding remarks

Summarizing, we have considered the problem of finding the optimal distribution in space of a composite biomorphic ceramic material that is constructed by periodically distributed constituents in an infinitesimal tracheidal microstructure. The macroscopic homogenized model is obtained by the homogenization approach assuming an asymptotic expansion of the solution of the nonhomogenized elasticity equation with a scale parameter close to zero. The design objective is to determine the microstructural geometric features in order to get an optimal performance of the material. The cost functional is subject to a set of equality and inequality constraints on the state variables (displacements with regard to the elasticity equation) and the design parameters (widths of the layers in the microcell). The computation of the homogenized elasticity coefficients plays a key role in our shape optimization problem since the homogenized equilibrium equation is considered as an equality constraint within the optimization procedure. Our adaptive mesh-refinement strategy is based on the Zienkiewicz–Zhu error estimator and yields satisfactory results as the numerical experiments show. We notice that our mathematical work and computational examples are supported by experimental investigations that provide both realistic model parameters as well as data for model validation.

Acknowledgements

This work has been partially supported by the German National Science Foundation (DFG) under Grant No. HO877/5-2. The second author has also been supported in part by the Bulgarian NSF under Grant No. I1001/2000.

References

[1] N. Bakhvalov, G. Panasenko, Averaging Processes in Periodic Media, Nauka, Moscow, 1984.
[2] M.P. Bendsøe, Optimization of Structural Topology, Shape, and Material, Springer, Berlin, Germany, 1995.
[3] A. Bensoussan, J.L. Lions, G. Papanicolaou, Asymptotic Analysis for Periodic Structures, Elsevier, Amsterdam, 1978.
[4] A.V. Fiacco, G.P. McCormick, Nonlinear Programming. Sequential Unconstrained Minimization Techniques, Wiley, New York, 1968 (republished by SIAM, Philadelphia, Pennsylvania, 1990).
[5] V.V. Jikov, S.M. Kozlov, O.A. Oleinik, Homogenization of Differential Operators and Integral Functionals, Springer, 1994.
[6] J. Sokolowski, J.-P. Zolesio, Introduction to shape optimization, Springer Series in Computational Mathematics, vol. 16, Springer, 1992.

[7] M.P. Bendsøe, N. Kikuchi, Generating optimal topologies in structural design using a homogenization method, Comput. Methods Appl. Mech. Eng. 71 (1988) 197–224.
[8] R.H. Byrd, M.E. Hribar, J. Nocedal, An interior point algorithm for large scale nonlinear programming, SIAM J. Optim. 9 (4) (1999) 877–900.
[9] C.E. Byrne, D.C. Nagle, Carbonization of wood for advanced materials applications, Carbon 35 (2) (1997) 259–266.
[10] C. Carstensen, S.A. Funken, Averaging technique for FE—a posteriori error control in elasticity. Part I. Conforming FEM, Comput. Methods Appl. Mech. Eng. 190 (2001) 2483–2498.
[11] A.S. El-Bakry, R.A. Tapia, T. Tsuchiya, Y. Zhang, On the formulation and theory of the Newton interior-point method for nonlinear programming, J. Optim. Theory Appl. 89 (1996) 507–541.
[12] K. Eriksson, D. Estep, P. Hansbo, C. Johnson, Introduction to adaptive methods for differential equations, Acta Num. (1995), 105–158.
[13] A. Forsgren, P.E. Gill, M.H. Wright, Interior methods for nonlinear optimization, SIAM Rev. 44 (4) (2002) 525–597.
[14] D.M. Gay, M.L. Overton, M.H. Wright, A primal–dual interior method for nonconvex nonlinear programming, in: Y. Yuan (Eds.), Advances in Nonlinear Programming, Kluwer, Dordrecht, 1998, pp. 31–56.
[15] P. Greil, T. Lifka, A. Kaindl, Biomorphic cellular silicon carbide ceramics from wood. I. Processing and microstructure. II. Mechanical properties, J. Eur. Ceram. Soc. 18 (1998) 1961–1973, and 1975–1983.
[16] R.H.W. Hoppe, S.I. Petrova, V. Schulz, Primal–dual Newton-type interior-point method for topology optimization, J. Optim. Theory Appl. 114 (3) (2002) 545–571.
[17] N. Kikuchi, K.Y. Chung, T. Torigaki, J.E. Taylor, Adaptive finite element methods for shape optimization of linearly elastic structures, Comput. Methods Appl. Mech. Eng. 57 (1986) 67–91.
[18] T. Ota, M. Takahashi, T. Hibi, M. Ozawa, S. Suzuki, Y. Hikichi, H. Suzuki, Biomimetic process for producing SiC wood, J. Am. Ceram. Soc. 78 (1995) 3409–3411.
[19] H. Sieber, C. Hoffmann, A. Kaindl, P. Greil, Biomorphic cellular ceramics, Adv. Eng. Mater. 2 (2000) 105–109.
[20] K. Suzuki, N. Kikuchi, A homogenization method for shape and topology optimization, Comput. Methods Appl. Mech. Eng. 93 (1991) 291–318.
[21] G. Wittum, On the convergence of multigrid methods with transforming smoothers. Theory with applications to the Navier–Stokes equations, Num. Math. 57 (1989) 15–38.
[22] O.C. Zienkiewicz, J.Z. Zhu, A simple error estimator and adaptive procedure for practical engineering analysis, Int. J. Num. Methods Eng. 24 (1987) 337–357.